UNIVERSITY OF BATH

Citation for published version:
Steele, IA, Kopac, D, Arnold, DM, Smith, RJ, Kobayashi, S, Jermak, HE, Mundell, CG, Gomboc, A, Guidorzi, C, Melandri, A & Japelj, J 2017, 'Polarimetry and Photometry of Gamma-Ray Bursts with RINGO2', *Astrophysical Journal*, vol. 843, pp. 143-158. https://doi.org/10.3847/1538-4357/aa79a2

DOI:
10.3847/1538-4357/aa79a2

Publication date:
2017

Document Version
Publisher's PDF, also known as Version of record

Link to publication

© American Astronomical Society. The final publication is available at IOP via https://doi.org/10.3847/1538-4357/aa79a2

University of Bath

Alternative formats
If you require this document in an alternative format, please contact:
openaccess@bath.ac.uk

General rights
Copyright and moral rights for the publications made accessible in the public portal are retained by the authors and/or other copyright owners and it is a condition of accessing publications that users recognise and abide by the legal requirements associated with these rights.

Take down policy
If you believe that this document breaches copyright please contact us providing details, and we will remove access to the work immediately and investigate your claim.

Download date: 05. May. 2023

The Astrophysical Journal, 843:143 (15pp), 2017 July 10 https://doi.org/10.3847/1538-4357/aa79a2
© 2017. The American Astronomical Society. All rights reserved.

Polarimetry and Photometry of Gamma-Ray Bursts with RINGO2

I. A. Steele[1], D. Kopač[1,2], D. M. Arnold [1], R. J. Smith[1], S. Kobayashi[1], H. E. Jermak[1,3], C. G. Mundell[4], A. Gomboc[5], C. Guidorzi[6], A. Melandri[7], and J. Japelj[8]
[1] Astrophysics Research Institute, Liverpool John Moores University, Liverpool, L3 5RF, UK
[2] Faculty of Mathematics and Physics, University of Ljubljana, Jadranska 19, Ljubljana 1000, Slovenia
[3] Department of Physics, Lancaster University, Bailrigg Campus, Lancaster, LA1 4YW, UK
[4] Department of Physics, University of Bath, Claverton Down, Bath, BA2 7AY, UK
[5] Centre for Astrophysics and Cosmology, University of Nova Gorica, Vipavska 11c, Ajdovščina 5270, Slovenia
[6] Department of Physics and Earth Science, University of Ferrara, Italy
[7] INAF-Osservatorio Astronomico di Brera, via E. Bianchi 36, I-23807 Merate (LC), Italy
[8] Anton Pannekoek Institute for Astronomy, University of Amsterdam, Science Park 904, 1098 XH Amsterdam, The Netherlands
Received 2016 December 12; revised 2017 June 6; accepted 2017 June 12; published 2017 July 14

Abstract

We present a catalog of early-time ($\sim 10^2 - 10^4$ s) photometry and polarimetry of all gamma-ray burst (GRB) optical afterglows observed with the RINGO2 imaging polarimeter on the Liverpool Telescope. Of the 19 optical afterglows observed, the following nine were bright enough to perform photometry and attempt polarimetry: GRB 100805A, GRB 101112A, GRB 110205A, GRB 110726A, GRB 120119A, GRB 120308A, GRB 120311A, GRB 120326A, and GRB 120327A. We present multiwavelength light curves for these 9 GRBs, together with estimates of their optical polarization degrees and/or limits. We carry out a thorough investigation of detection probabilities, instrumental properties, and systematics. Using two independent methods, we confirm previous reports of significant polarization in GRB 110205A and 120308A, and report the new detection of $P = 6^{+3}_{-2}\%$ in GRB101112A. We discuss the results for the sample in the context of the reverse- and forward-shock afterglow scenario, and show that GRBs with detectable optical polarization at early time have clearly identifiable signatures of reverse-shock emission in their optical light curves. This supports the idea that GRB ejecta contain large-scale magnetic fields, and it highlights the importance of rapid-response polarimetry.

Key words: gamma-ray burst: general – magnetic fields – polarization

Supporting material: machine-readable table

1. Introduction

Almost half a century since the discovery of gamma-ray bursts (GRBs), these cosmic explosions remain puzzling, particularly regarding the origin and role of magnetic fields in driving the explosion (Granot et al. 2015). Relativistic outflow associated with GRB events is conventionally assumed to be a baryonic jet, producing synchrotron emission with tangled magnetic fields generated locally by instabilities in shocks (Piran 1999; Zhang & Mészáros 2004). However, recent polarization observations indicate the existence of large-scale magnetic fields in the outflow (Steele et al. 2009; Yonetoku et al. 2011; Mundell et al. 2013). The rotation of a black hole and an accretion disk (i.e., the standard GRB central engine) might cause a helical outgoing magnetohydrodynamic wave that accelerates material frozen into the field lines. In such magnetic models, the outflow is expected to be threaded with globally ordered magnetic fields (Komissarov et al. 2009).

Because of their cosmological distances, measurement of the degree of polarization (P) and the electric vector polarization angle (EVPA) of the light is the only direct probe of magnetic fields in GRB jets. Early polarimetric studies focused on the evolution of polarization around a jet break to give constraints on the collimation of a jet and the angular dependence of the energy distribution (Ghisellini & Lazzati 1999; Sari 1999; Rossi et al. 2004). Jet breaks are expected to occur at $\gtrsim$1 day after GRB triggers, and observed polarization degrees at such late times are rather low at only a few percent (Covino et al. 1999; Wijers et al. 1999).

Since the late-time afterglow is emitted from shocked ambient medium (i.e., forward shock), rather than the original ejecta from the GRB central engine, it is insensitive to the jet acceleration process. The magnetic properties of the original ejecta can be examined only through the investigation of the prompt gamma-rays or reverse-shock emission. This requires polarization measurements of the GRBs themselves or the early afterglow ($\lesssim$30 minutes). For this purpose, RINGO and RINGO2 imaging polarimeters on the Liverpool Telescope (LT) were developed, with which we can measure the polarization of afterglow just a few minutes after a GRB trigger. Since synchrotron emission is expected to be linearly polarized, only linear polarization measurements are discussed in this paper (see Wiersema et al. 2014 for a recent detection of circular polarization and Nava et al. (2016) for discussion of its implication). Linear polarization can also be produced by the inverse-Compton scattering process (Lazzati et al. 2004; Lin et al. 2017).

In this paper we present the complete catalog of photometry and polarimetry of GRBs observed with the RINGO2 imaging polarimeter on LT. Of the 19 optical afterglows observed, nine were bright enough to perform photometry and attempt polarimetry. Additional photometric measurements obtained with RATCam (Steele 2001) on the same telescope are also presented. RINGO2 technical details, calibration, and the data reduction process are discussed in Section 2. In Section 3 we list the GRBs observed during RINGO2 operation, and in Sections 4 and 5 we present the photometry and polarimetry

results of the sample. A discussion and interpretation follows in Section 6, and we summarize our conclusions in Section 7.

2. RINGO2

2.1. Telescope and Instrument Description

The LT is a 2.0 meter fully robotic telescope at the Observatorio del Roque de los Muchachos, La Palma (Steele et al. 2004). It can host multiple instruments with a rapid change time (<30 s) and is optimized for time-domain astrophysics, including the rapid automated follow-up of transient sources such as GRBs (Guidorzi et al. 2006).

RINGO2 (Steele et al. 2010) was operational on LT from 2010 August 1 to 2012 October 26. Re-imaging optics gave the instrument a field of view of 4 × 4 arcmin. It used a polarizer rotating at ∼1 Hz to modulate the incoming beam from the telescope and a fast-readout low-noise electron-multiplying CCD (EMCCD) camera to sample the modulated image. Readout of the camera was electronically synchronized to the polarizer angle such that exactly eight images were obtained for a single rotation. By analysis of the relative intensities of a source within the eight images, the degree of polarization could be determined.

All data from RINGO2 are pipeline reduced in the telescope's computer system to remove the standard instrumental signatures associated with CCD imaging. This comprises dark subtraction and flat-field division. Owing to the short individual exposure times (∼125 ms), an observation will comprise many repeated exposures at each of the eight rotor positions. Each rotor position exposure is therefore combined in longer (1–10 minute) time bins to make eight mean images (one per rotor position). A world coordinate system (WCS) fit is then added to the FITS headers, and the mean images are transferred to the user for analysis.

2.2. Extraction of Polarization Signal

To extract the polarization signal for an object from RINGO2 data it is necessary to measure the relative number of (sky-subtracted) counts in each of the eight mean images for that object. Because of the field-position-dependent point-spread function (PSF) caused by the RINGO2 re-imaging optics, PSF fitting was not appropriate for this measurement. Instead, we used aperture photometry with an aperture size of 3.5 arcsec diameter. This value is the mean location of the maximum in a signal-to-noise ratio versus aperture size plot for multiple observations of 10 objects in the field of the polarimetric standard HD212311. The objects had apparent magnitudes in the range 8 to 17. Extraction of the counts for every source on every image was automated using SExtractor (Bertin & Arnouts 1996) with local sky subtraction. More detailed descriptions of these procedures are presented in Jermak et al. (2016), Jermak (2016), and Arnold (2017).

For every object in the eight-image set, the measured Stokes q_m and u_m parameters and associated errors (based on the photon statistics) are calculated from the sky-subtracted counts following the prescription presented by Clarke & Neumayer (2002). These results are stored in a MySQL database along with other FITS header data such as observation date and telescope and environmental information. This allowed checks to be made for any trends with quantities such as lunar phase (Figure 1) in the data. No such trends were found (see Arnold (2017) for more details).

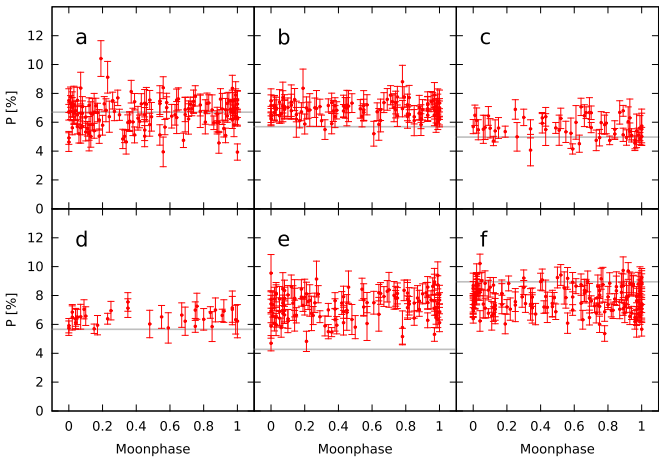

Figure 1. Observed polarization vs. lunar phase for the polarized standard stars (a) BD +49 389, (b) BD+64 106, (c) HD 155528, (d) Hiltner 960, (e) BD +25 727, and (f) VI Cyg #12. The horizontal gray lines are catalog polarizations from Schmidt et al. (1992) and Turnshek et al. (1990)

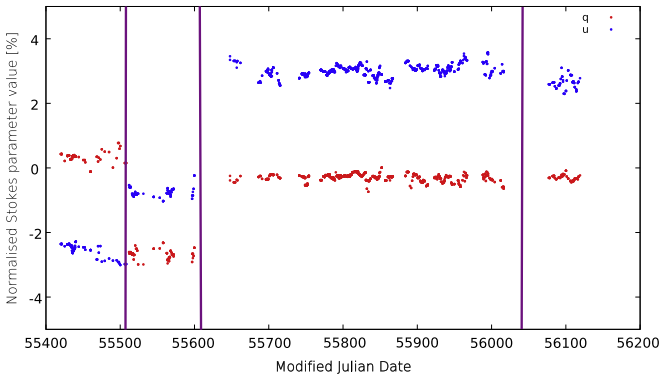

Figure 2. Time evolution of the measured RINGO2 instrumental polarization zero-points. Blue points indicate u_0 and red points q_0. Times of instrument hardware changes are indicated by vertical lines.

Conversion of the measured Stokes q_m and u_m parameters to the degree of polarization (P) and electric vector polarization angle (EVPA) is carried out via the standard equations

$$q = q_m - q_0, \tag{1}$$

$$u = u_m - u_0, \tag{2}$$

$$P = \frac{\sqrt{q^2 + u^2}}{D}, \tag{3}$$

$$\mathrm{EVPA} = \frac{1}{2}\arctan\frac{u}{q} + \mathrm{SKYPA} + \mathrm{K}, \tag{4}$$

where q_0 and u_0 are measures of the instrumental polarization. q_0 and u_0 were determined using our observations of zero-polarized standard stars (Schmidt et al. 1992). Figure 2 shows the results of this analysis as a function of time. The final derived quantities based on combining data from all of the standards are presented in Table 1. Step changes in these quantities are associated with instrument servicing activity. Except for this, they remain constant.

Although it rotates between q_0 and u_0 with hardware servicing activities, the mean measured instrumental polarization over the entire RINGO2 lifetime was a nearly constant 2.9%, with a standard deviation of 0.4%. This (relatively high)

Table 1
Mean Stokes q and u Zero-points and EVPA Zero-point K for RINGO2 Periods of Operation

MJD Range	Date Range	q_m	sd(q_m)	u_m	sd(u_m)	K	sd(K)
55418–55510	20100810–20101110	+0.0030 ± 0.0006	0.0031	−0.0250 ± 0.0006	0.0041	126°	4°
55511–55607	20101111–20110215	−0.0261 ± 0.0005	0.0047	−0.0074 ± 0.0005	0.0031	171°	3°
55640–56045	20110320–20120428	−0.0030 ± 0.0002	0.0025	+0.0297 ± 0.0003	0.0036	41°	3°
56045–56226	20120428–20121026	−0.0031 ± 0.0004	0.0017	+0.0264 ± 0.0005	0.0041	42°	2°

Note. *pm* Errors are the standard error on the mean, whereas sd() quantities are the standard deviation of the sample.

instrumental polarization is mainly caused by the instrument being fed from a 45° reflecting mirror in the telescope.

The quantity D is a measure of the instrumental depolarization caused by the imperfect contrast ratio of the polarizer. It was calibrated by observations of polarized standard stars (Turnshek et al. 1990; Schmidt et al. 1992) over the entire observation period and determined to be 0.76 ± 0.01. When this value is used to correct the measured instrumental polarization, a value of 3.8% is found, which is in line with the expectation for a 45° reflecting mirror (Cox 1976).

The quantity SKYPA is the telescope Cassegrain axis sky position angle (measured east of north) and K a calibration offset to that position angle that combines the angles between the orientation of the polarizer, the telescope focal plane, and the trigger position of the angle measuring sensor. K was determined using our polarized standard star observations and was found (Table 1) to be stable within each observation period to within 4° (standard deviation).

An analysis of the position dependence of polarization in the instrument derived from observations of the twilight sky is presented in the supplementary material of Mundell et al. (2013). This shows that this effect is <1.5% of the measured polarization (so for example on a 10% polarized source, it would introduce a maximum error of 0.15%).

Since q and u are constructed by linear combinations of count values that are subject to Poisson counting statistics, their error distributions will be normally distributed (symmetrical) and can be calculated by standard error propagation theory (Clarke & Neumayer 2002). However, for P and EVPA, the process is more complex. In particular P, being a quantity that is always positive, Equation (3) will have a Rayleigh distribution (Papoulis 1984). This means that it will have an asymmetric distribution of errors. The value of P itself will therefore also suffer from a polarization bias, where noise in q and u will generate a false increase in the P value (Simmons & Stewart 1985). A similar problem also affects EVPA measurements (Naghizadeh-Khouei & Clarke 1993). These problems must be particularly addressed at low values of P where the error distribution becomes increasingly asymmetric. They are taken into account in the analysis of our GRB results presented in Section 5.

2.3. Photometric Reduction and Calibration

In addition to the RINGO2 observations, optical band photometry of each burst was carried out using the RATCam CCD imaging camera in intervals between and after the RINGO2 observations. These photometric observations were typically made using either $g'r'i'$ or $r'i'z'$ filter sequences and provide multicolor light curves that cover a longer time baseline than the RINGO2 observations alone. Conventional circular-aperture photometry was performed with sky flux determined locally for each source from an annular aperture surrounding the target. Zero-points were derived from RATCam observations of SDSS secondary standards (Smith et al. 2002) taken on the same night. Instrumental zero-points in each filter were obtained as an average for all the SDSS standards available, which amounted to between two and five different stars per night. Rather than apply this zero-point directly to photometry of the GRB afterglow, a zero-point was established for each GRB frame as the average for several sources detected in that frame with comparable brightness to the GRB afterglow. The number of available stars varied between two and seven. Any sources that showed statistically significant variation during the period of observation, whether that be genuine variability or simply poor data, were rejected before deriving the instrumental zero-point for that image. The optical transient magnitude was finally obtained by aperture photometry relative to that ensemble average of between two and five field stars.

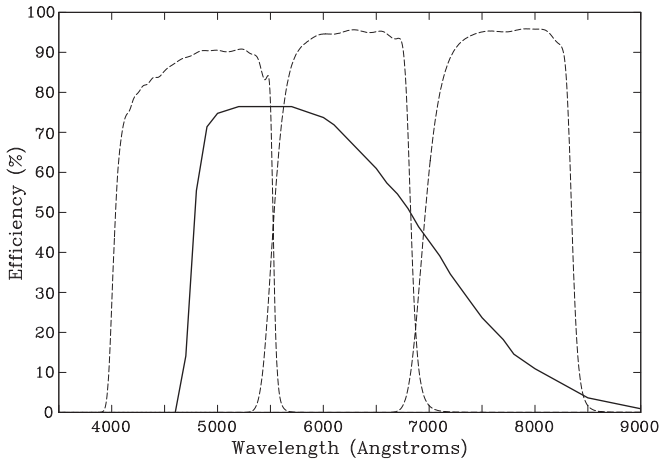

Figure 3. RINGO2 filter throughput (solid line) compared to SDSS-g', r', i' filters (dashed lines from left to right).

No color corrections have been included because detailed transformations between RATCam and the SDSS calibration telescope are not available. However, the RATCam filters are sufficiently close to the SDSS passbands that errors are expected to be substantially smaller than the typical statistical photon-counting errors in our observations. The RATCam observers' documentation cites color corrections of less than $0.05(r' - i')$, implying less than 0.025 mag for sources of typical stellar colors.

Summing the eight polarized images in a RINGO2 observation provides unpolarized photometry. The wavelength range is determined by a custom filter comprised of 3 mm Schott GG475 cemented to 2 mm Schott KG3, which gives an approximate wavelength range of 4750–7100 Å (2350 Å FWHM). The filter bandpass is shown in Figure 3 where it can be compared to the SDSS filter bandpasses (Smith et al. 2002). For each afterglow we therefore have both multi-filter RATCam and single-filter RINGO2 imaging. The primary objective here is to transform the RINGO2 data onto a similar reference frame as the RATCam data and allow direct comparison in a single light curve.

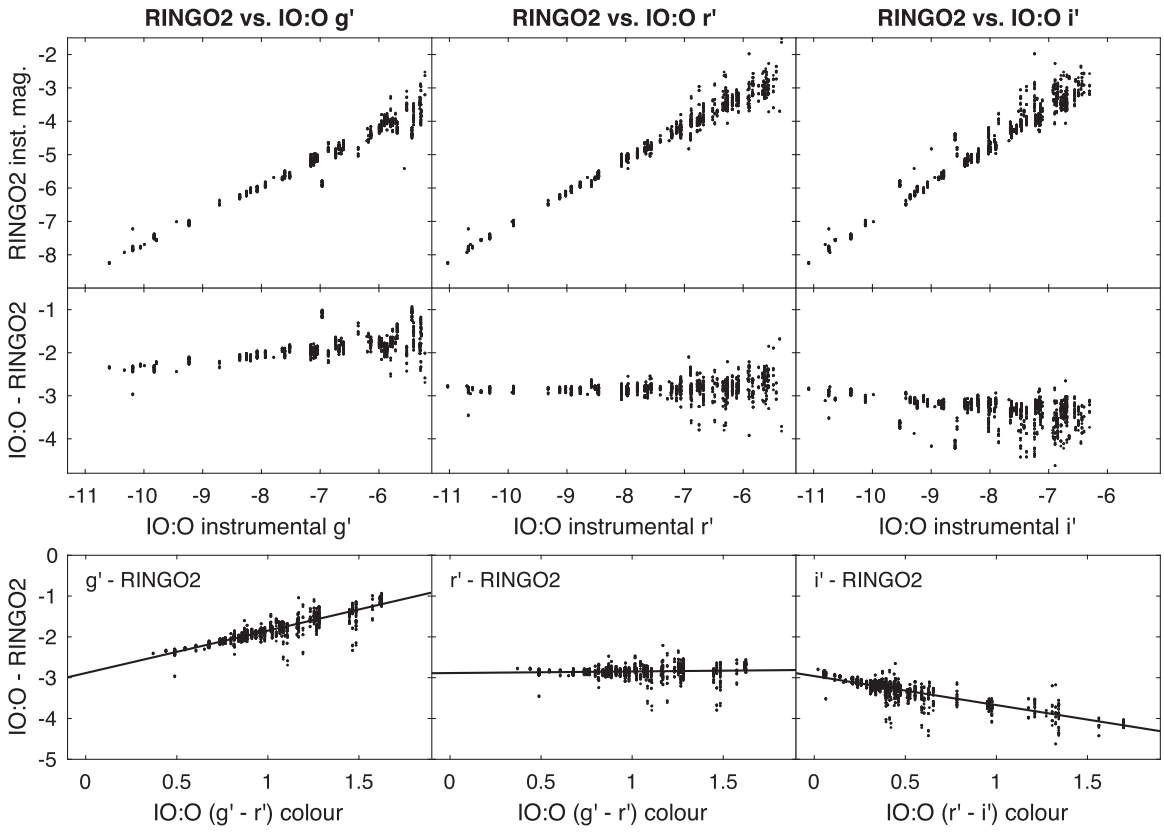

Figure 4. Aperture photometry of all stars in the field surrounding star BD+32 3739 (HD 331891). RINGO2 data are taken from observations of this standard star on all photometric nights between 2012 June 3 and 2012 October 26. The eight RINGO2 images at each epoch are coadded to create an unpolarized image. The comparison IO:O data are a single epoch, obtained on the night of 2013 September 4. All numbers are simple instrumental magnitudes calculated as $-2.5\ \log_{10}$(counts). The left panels compare RINGO2 to IO:O g' filter, the central column is RINGO2 and IO:O r', and the right panels show IO:O i'. The top row directly compares the instrumental magnitudes from the two instruments. The middle row plots the magnitude difference between RINGO2 and various IO:O filters, effectively the zero-point difference between the instruments, which is shown to be independent of magnitude for filter r'. The bottom row derives zero-point color transformations between the RINGO2 filter and the various SDSS-type filters. Again, r' is seen to be a good match to RINGO2 without applying any color correction. The clumpy distribution of points is caused by a single IO:O observation of each star, which is compared to 54 epochs of RINGO2 observations.

As part of its routine calibration program, RINGO2 observed zero and non-zero polarized standard objects (Schmidt et al. 1992) several times per night throughout its period of operation. To characterize the non-standard filter, observations have also been made of the same fields with the CCD imager IO:O (Steele et al. 2014), which replaced the decommissioned RATCam in 2012 June. IO:O has a filter wheel and full suite of SDSS-type filters. These are polarimetric, not photometric, standards, so the fields do not contain established references intended to develop an absolute photometric calibration. However, we can use them to compare raw instrumental magnitudes of the many field stars in the various SDSS filters with RINGO2 magnitudes. Figure 4 demonstrates that SDSS r' provides an excellent match to RINGO2's natural photometric system. We therefore use SDSS r' as the basis for the relative photometric calibration of our GRB afterglow light-curves with no need to apply color corrections.

After selecting SDSS r' as the best comparison reference, photometry was extracted from the RINGO2 frames following the same procedures as the RATCam data described above.

For both RATCam and RINGO2, the magnitudes of the optical transient (OT) in various bands were corrected for Galactic extinction using maps from Schlafly & Finkbeiner (2011).[9] Finally we converted into flux densities using flux zero-points provided in Fukugita et al. (1995).

[9] http://ned.ipac.caltech.edu/forms/calculator.html

3. Observations

Between 2010 and 2012, 19 optical afterglows were observed with the RINGO2 polarimeter. Table 2 shows observational properties of the complete sample, the time of the RINGO2 observations, and the mid-time optical (r' equivalent band) magnitude of the source. In most cases, the LT and RINGO2 response time was 2–3 minutes, but only one event (GRB 101112A) was brighter than ∼16th magnitude during these observations. Of the 19 afterglows, 10 were too faint during the time of the RINGO2 observations to perform photometry and thus polarimetry. For the remaining nine events, we were able to perform both photometry and attempt polarimetry. The results for GRB 120308A (Mundell et al. 2013) and a preliminary analysis of GRB 110205A (Cucchiara et al. 2011b) have already been presented separately.

Individual details of the RINGO2 and RATCam photometric reduction for each GRB are provided in Section 4. The RINGO2 polarimetric results are presented in Section 5.

4. Results: Photometry

In the following subsections we summarize photometric reduction and calibration details for nine GRBs from the RINGO2 sample, to obtain the complete light curves that are tabulated in Table 5. All data were processed according the general procedures described above and only particular features

Table 2
The Complete Sample of 19 GRB Afterglows Observed with RINGO2

GRB	$t - T_0$ (s)	r' Mag. at Mid-time	GCN Reference
100802A	116–295	18.79 ± 0.64	
100805A	140–320	17.29 ± 0.13	
	1020–1198	18.76 ± 0.57	
101112A	176–355	15.77 ± 0.03	
	715–893	16.61 ± 0.05	
110106B	697–875	>22.5 at 2620 s	Guidorzi et al. (2011)
110205A	422–722	16.92 ± 0.68	
	3026–3506	16.37 ± 0.07	
110402A	214–813	∼20.8 at 1680 s	Mundell et al. (2011)
110520A	142–741	>19.0 at 215 s	Klotz et al. (2011)
	1081–1259	>19.7 at 1879 s	Lacluyze et al. (2011)
110726A	191–783	17.99 ± 0.11	
	4582–5180	⋯	
120119A	194–793	17.65 ± 0.04	
120305A	154–752	>21.3 at 840 s	Virgili et al. (2012)
120308A	240–838	16.51 ± 0.03	
120311A	181–779	18.41 ± 0.18	
	3818–4416	⋯	
120324A	183–781	>20.3 at 840 s	Guidorzi & Melandri (2012)
120326A	216–872	18.88 ± 0.14	
120327A	1664–2263	16.66 ± 0.03	
	2605–2784	17.11 ± 0.05	
120514A	556–1155	>18.1 at 721 s	Klotz et al. (2012)
120521C	777–1375	>21.5 at 2100 s	Bersier (2012)
120711B	157–755	>21.7 at 42469 s	Kuroda et al. (2012)
	1249–1847	⋯	
	2403–3001	⋯	
120805A	215–813	∼20.9 at 960 s	Guidorzi & Mundell (2012)

Note. Photometric errors quoted are the statistical error on the observation. In particular, those calibrated with respect to USNO-B1 catalogs (GRB 110726A, GRB 120326A) show larger systematic errors (typically 0.3 mag). All bursts were initially detected by *Swift*, except for GRB101112A, which was detected by *INTEGRAL*. The second column shows the time of RINGO2 observations with respect to the gamma-ray trigger, and the third column lists the r' band optical magnitude at the mid-time of the RINGO2 epoch. When no r' magnitude with error is reported, the source was too faint to be observed with RINGO2 and a limit or measurement from the GCN report nearest in time is given.

of individual data sets are described here. In addition, high-energy properties from the literature are also provided for all 9 GRBs from the sample.

4.1. GRB 100805A

RATCam observations were obtained in SDSS g', r' and i'. Final OT photometry is quoted with respect to a zero-point established by the average of four field stars. Galactic extinctions applied were $A_{g'} = 0.61$, $A_{r'} = 0.42$, and $A_{i'} = 0.31$.

The gamma-ray duration for this GRB in 15–350 keV band is $T_{90} = 16.7 \pm 3.1$ s (Lien et al. 2016), while the photometric redshift obtained from the UVOT data is $z \approx 1.3$ (Holland & Hoversten 2010).

4.2. GRB 101112A

The optical afterglow was discovered by Guidorzi et al. (2010). RATCam data are available in SDSS g', r' and i' filters. Three field stars were averaged to give the frame reference in the OT images. Galactic extinction corrections are $A_{g'} = 0.50$, $A_{r'} = 0.35$, and $A_{i'} = 0.26$.

The gamma-ray duration for this GRB in 50–300 keV band is $T_{90} = 9.2$ s (Goldstein 2010), while the upper limit on the photometric redshift (given the detection in g' band) is $z \lesssim 3.5$.

4.3. GRB 110205A

RATCam data in SDSS g', r' and i', and SWIFT UVOT u, b and v magnitudes were all obtained from Cucchiara et al. (2011b). Photometry from the LT RATCam data was rechecked following the same procedures as for the other targets presented here, and it was found to be consistent with the published data. The additional UVOT data from Cucchiara et al. (2011b) allow better coverage across the optical peak. Galactic extinction corrections are $A_V = 0.04$, $A_R = 0.03$, $A_{g'} = 0.05$, $A_{r'} = 0.03$, $A_{i'} = 0.02$, $A_u = 0.06$, $A_b = 0.05$, and $A_v = 0.04$. The SDSS magnitudes were converted into flux densities as previously described and the UVOT magnitudes using flux zero-points provided in Breeveld et al. (2011).

The gamma-ray duration for this GRB in 15–350 keV band is $T_{90} = 249 \pm 15$ s (Lien et al. 2016), while the redshift is $z = 2.22$ (Cenko et al. 2011).

4.4. GRB 110726A

RATCam data in g', r' and i' filters were obtained, but same-night observations of photometric standards were not available. Instead, B2, R2, and I magnitudes from USNO-B1 were converted into SDSS g', r', and i' magnitudes using Jordi et al. (2006) and combined with aperture photometry of four nearby field stars to provide a zero-point on each image. The errors tabulated in Table 5 are statistical estimates (consistent with our treatment of the other afterglows) that do not take into account that USNO-B1 has a typical spatially varying systematic photometric error (1σ) of ∼0.3 magnitude. The Galactic extinction corrections were $A_V = 0.21$, $A_R = 0.17$, $A_{g'} = 0.26$, $A_{r'} = 0.18$, and $A_{i'} = 0.13$.

The gamma-ray duration for this GRB in 15–350 keV band is $T_{90} = 5.2 \pm 1.1$ s (Lien et al. 2016), while the redshift range is $1.036 < z < 2.7$ (Cucchiara et al. 2011a).

4.5. GRB 120119A

The RATCam observations used SDSS r', i' and z' filters. Our photometry is found to be consistent with data published in Morgan et al. (2014). Additional PROMPT data in R and I filters from that paper were used to sample the light curve more densely at early and late times. Galactic extinction corrections are $A_R = 0.23$, $A_I = 0.16$, $A_{r'} = 0.25$, $A_{i'} = 0.18$, and $A_{z'} = 0.14$.

The gamma-ray duration for this GRB in 15–350 keV band is $T_{90} = 68.0 \pm 7.1$ s (Lien et al. 2016), while the redshift is $z = 1.728$ (Cucchiara & Prochaska 2012).

4.6. GRB 120308A

The RATcam observations used r', i' and z' filters. Photometry was performed using the procedures outlined above and have already been published in Mundell et al. (2013). As an additional cross-check, this paper also derived magnitudes using USNO-B1 magnitudes for which we transformed B2, R2, and I magnitudes to SDSS r', i' and z' magnitudes using Jordi et al. (2006). The results were

consistent within 1σ error bars. The Galactic extinction maps give $A_{r'} = 0.09$, $A_{i'} = 0.07$, and $A_{z'} = 0.05$.

The gamma-ray duration for this GRB in 15–350 keV band is $T_{90} = 61 \pm 17$ s (Lien et al. 2016), while the derived photometric redshift is $z \approx 2.2$ (Mundell et al. 2013).

4.7. GRB 120311A

RATCam observations used r', i' and z' filters, and zero-points were derived from the average of three field stars. Galactic extinction values for the field are $A_{r'} = 0.31$, $A_{i'} = 0.23$, and $A_{z'} = 0.17$.

The gamma-ray duration for this GRB in 15–350 keV band is $T_{90} = 3.5 \pm 0.8$ s (Lien et al. 2016), while the derived upper limit on the photometric redshift is $z \lesssim 3$ (D'Avanzo et al. 2012).

4.8. GRB 120326A

RATCam data in r', i', and z' filters were obtained from Melandri et al. (2014). Same-night observations of photometric standards were not available so each frame's zero-point was derived by averaging nearby field stars using USNO-B1 magnitudes as the reference. See the note regarding USNO-B1 errors for GRB 110726A. The Galactic extinction corrections were $A_V = 0.14$, $A_R = 0.11$, $A_{r'} = 0.12$, $A_{i'} = 0.09$, and $A_{z'} = 0.06$.

The gamma-ray duration for this GRB in 15–350 keV band is $T_{90} = 69.5 \pm 8.2$ s (Lien et al. 2016), while the redshift is $z = 1.798$ (Tello et al. 2012).

4.9. GRB 120327A

RATCam observations were in r', i', and z' filters and zero-points derived from an average of three field stars. Galactic extinction correction for the field is $A_{r'} = 0.76$, $A_{i'} = 0.57$, and $A_{z'} = 0.42$.

The gamma-ray duration for this GRB in 15–350 keV band is $T_{90} = 63.5 \pm 7.0$ s (Lien et al. 2016), while the redshift is $z = 2.81$ (Perley & Tanvir 2012).

5. Results: Polarimetry

We derived q and u values and their associated errors for all of the objects in all of the RINGO2 GRB frames following the procedure outlined in Section 2.2. These are presented in Figure 5 as a function of apparent magnitude for all of the objects in the sample (except for GRB 120308A, where we have already presented such a plot in Mundell et al. 2013). The GRB measurements are indicated by red symbols. In most cases the red symbols are within the general distribution of points, but in some cases (GRB 10112A and 110205A) there is an apparent offset indicating a possible significant polarization detection.

To investigate the significance of these possible detections, we needed to consider the combination of information contained in both the q and u distributions. To do this, we used two independent and complementary methods. Our first method compared the calculated P value (Equation (3)) of the afterglow to all other sources in the field to test if the transient differs significantly from the population. Our second method used just the afterglow data itself and tested the null hypothesis that the measured P value was consistent with the scatter in its measured counts in the eight images and therefore no detection could be claimed.

We note that the RINGO2 data on GRB 110205A were originally presented in Cucchiara et al. (2011b), who gave an upper limit of $P < 16\%$ at the first epoch (240–840 s) and $P = 3.6^{+2.6}_{-3.6}\%$ in the second epoch (3047–3645 s). The enhanced analysis presented in the following sections is statistically consistent with these values, but does formally give a marginal detection for the first epoch. We also note that we originally presented results for GRB 120308A in Mundell et al. (2013). In this case although we reanalyzed the data along with the other bursts presented here, no changes to the results originally presented were found. For this reason we do not plot the data for that burst in Figures 5–8 as corresponding figures are already published there. The results for this burst are included in all of our tabular material, however, and in the discussion in Section 6.

5.1. Initial Analysis

In Figure 6 we plot the Stokes q versus u parameter for all of the detected sources in each GRB observation. For the GRB (red points) we also plot the error bars. The plots are generally characterized by a central "blob" of points near q, $u = 0.0$, 0.0 with the GRB often somewhat offset. In most cases the error bars indicate the GRB is at least consistent with no polarization. However, the cases of GRB10112A and 110205A are not so clear, especially at their first epochs of observation. In order to make an initial assessment of whether the offset of the GRB from the majority of other sources indicates a detection, we must take into account that every source will have different error bars (not plotted for clarity–see Figure 5 for the individual error bars on q and u.)

Since the polarimetric error is a function of total counts for each individual source in the frame, we investigated the distribution of the measured polarization of every source in a particular frame as a function of magnitude. For this analysis the polarimetric error on every source was calculated based on its individual q and u errors via a simple Monte Carlo error analysis. As described in Section 2.2, the errors on q and u are expected to have a normal (Gaussian) distribution and can be calculated by standard photon-counting statistics and error propagation theory (Clarke & Neumayer 2002).

For computational efficiency, in this initial analysis, the ratio u/q was assumed to be fixed to its measured value for each source in the frame. In other words, we assumed the measured EVPA for each source in the frame was correct (although different for each source). For each source a range of simulated P values from 0.01% to 70.00% was then stepped through. For each P value, corresponding q and u values were calculated (based on the EVPA). The Python numpy.randn Gaussian-weighted random number generator was then used to generate two separate 1000 value distributions centered on the calculated q and u values with standard deviations equal to the error estimated on each quantity calculated using Clarke & Neumayer (2002). These q and u distributions were then combined using Equation (3) to calculate a simulated P distribution, which was examined to see if the observed P lay within its 1σ limits and therefore the simulated P was "valid." The maximum and minimum valid P values after stepping through the whole range of simulated P therefore gave the error bars for that particular source. Tests showed that this procedure gives identical results to the graphical method presented in Simmons & Stewart (1985).

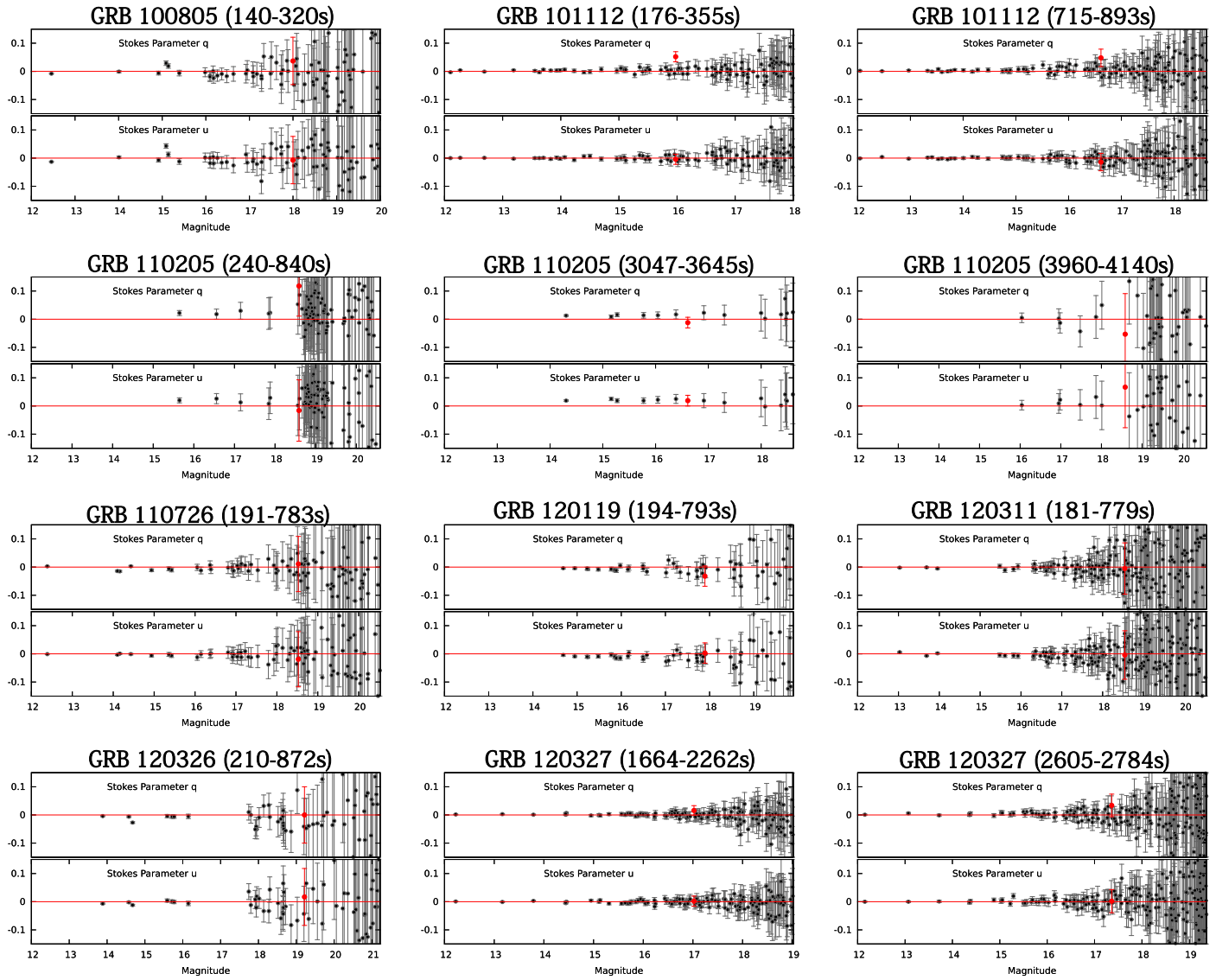

Figure 5. Stokes q and u parameters for the GRB sample (excluding GRB 120308A) as a function of apparent magnitude. In each plot the red point indicates the GRB and the black points are the other objects in the same frame. The q and u values have been corrected for instrumental polarization using the measured instrumental zero-points. The data have not been corrected for instrumental depolarization.

The results of this analysis are presented in Figure 7. As expected, the figure shows an increase in polarimetric error for fainter sources. However, it can also be seen that the apparent measured P value (calculated via Equation (3)) also increases for fainter sources. This is not real and is an example of polarimteric bias. As the signal-to-noise ratio decreases, the noise is converted into signal via the nonlinear nature of Equation (3).

Figure 7 shows that in general the GRBs are located within the expected noise at their measured magnitude level and therefore no claim of polarization detection can be made. However, both epochs of GRB 101112A and the first epoch of 110205A show the GRB located offset from the general cloud of points, indicating a possible polarization detection.

5.2. Permutation Analysis of Detection Probabilities

In order to investigate the detection probabilities more thoroughly, we therefore used our second method. This is a "permutation analysis" of the set of eight measured counts for each GRB prior to their conversion to Stokes parameters. To do this, we first had to remove the imprinted signal of instrumental polarization from the measured counts. This signal can be characterized by a response array of eight values. It is calculated for each of the eight rotor positions by averaging the normalized counts in all of our observations of zero-polarized standards to create an eight-value response array. Dividing this eight-value response array into the measured eight count values for the GRB then removes the effect of instrumental polarization (see Steele et al. (2006) for more details of this alternative approach to instrumental polarization correction to that done in the qu plane.)

Following this, we constructed all (8–1)! permutations of the ordering of the corrected count values to generate 5040 different sets of eight flux values. These sets have similar noise characteristics to the original data, being constructed directly from it. We then measured the polarization degree from each of these sets, and computed the ranking of the measured polarization of the GRB within all of the sets constructed from that GRBs reordered data. If the measured polarization were

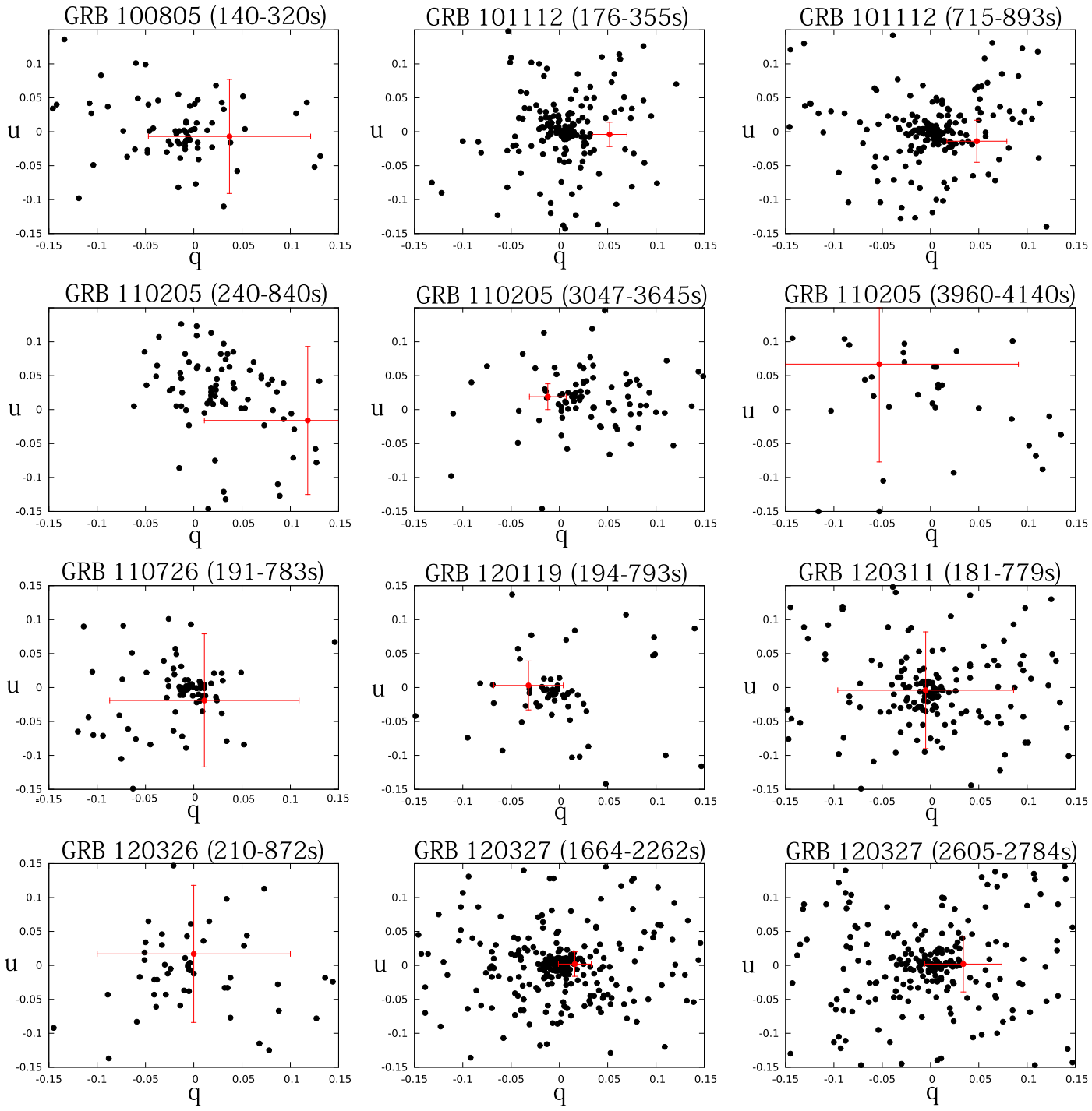

Figure 6. Stokes q vs. u parameters for the GRB sample (excluding GRB 120308A). The red point (with error bars) indicates the GRB, and the black points (without error bars) are the other objects in the same frame. The q and u values have been corrected for instrumental polarization using the measured instrumental zero-points. The data have not been corrected for instrumental depolarization.

simply a result of noise superimposed on a zero-polarized object, we would expect the measured polarization to lie randomly within the distribution of polarization values. This is therefore a test of the hypothesis that the polarization signal is non-zero.

The results of our analysis are presented in Figure 8 and Table 3. The ranks expressed as a fraction of the total number of permutations are equivalent to a probability that the measured GRB polarization is not the result of random noise. All epochs of measurement in GRB120308A, the first and second epoch of GRB 101112A, and the first epoch of GRB 110205A have a probability $p(=1 - \text{rank}) < 0.1$ of being consistent with zero percent polarization. No other bursts have detections that are not consistent with zero polarization at our confidence limit. This result is entirely consistent with the results from our first method analysis, and gives us confidence in our approach. We note that (except for GRB120308A, for which the non-zero polarization confidence is very high) we have three out of 12 measurements with $p < 0.1$. A binomial analysis shows the probability of zero polarization for all three measurements is 11%, making the conservative assumption of $p = 0.1$ in all cases.

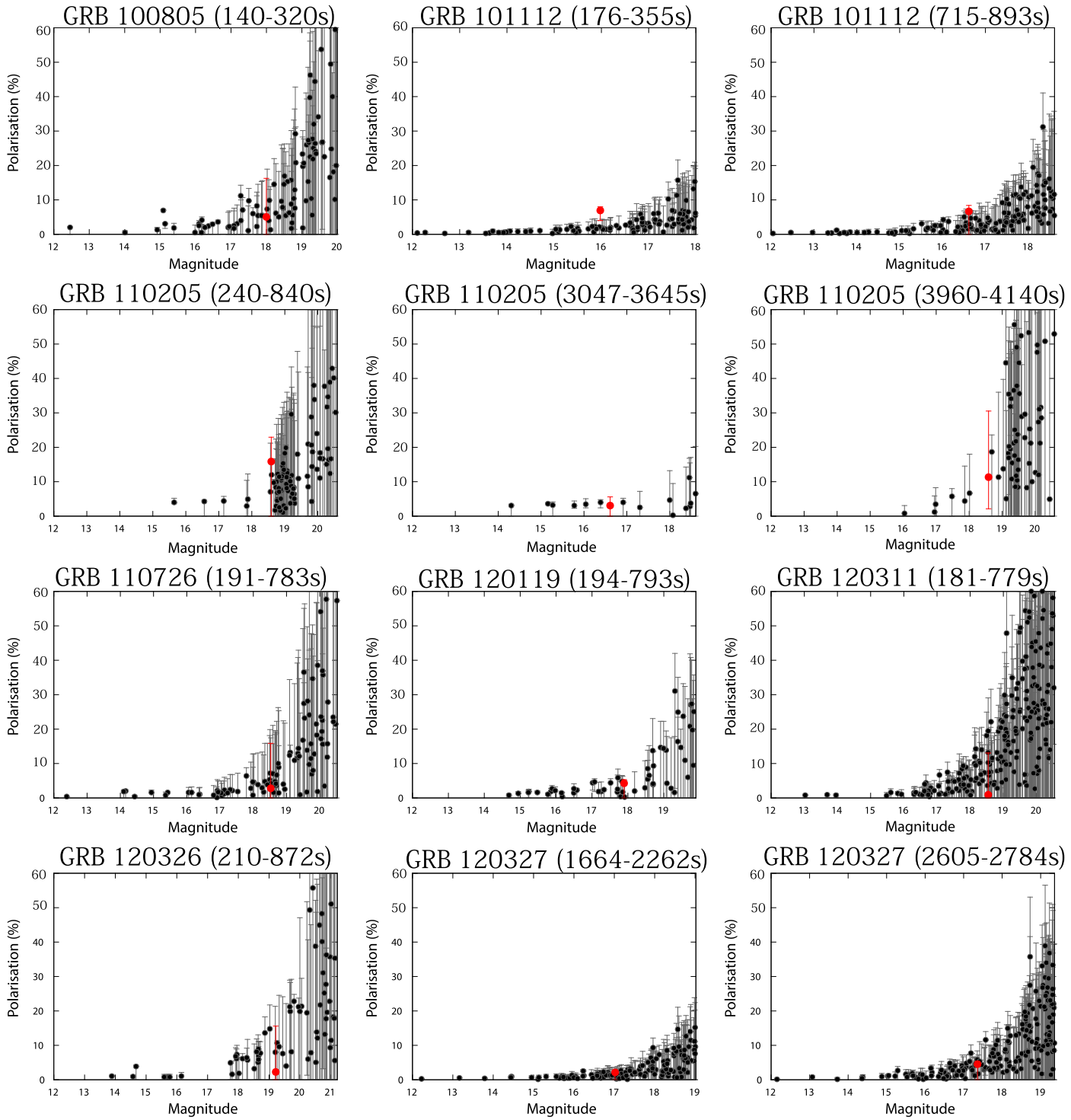

Figure 7. Observed polarization for GRBs (red points) and the other objects in the same frame (black points) as a function of magnitude. The magnitude is derived directly from the count rate of each object assuming a constant zero-point and is therefore not corrected for variations in sky transparency between different frames. The data are corrected for instrumental polarization and depolarization. The error bars are calculated from a Monte Carlo simulation based on simulating a range of P from 0.01 to 70.00% for each object and then generating a distribution of q and u values and hence a distribution of simulated possible measured P values corresponding to the input distribution. If the observed P lies in the 14th–86th percentile (corresponding to 1σ for a Gaussian distribution), then it is flagged as a possible true P value. The highest and lowest possible P values therefore give the error bar. As the count rate decreases, both the polarimetric error and polarization value increase. The apparent increase in polarization value is the effect of polarization bias where noise is transformed into signal via the polarization Equation (3).

5.3. Final Polarization Values

To determine the final polarization values and error bars for our polarization detections of the GRB optical counterparts, and the upper limits in the case where no positive polarization detection could be made, we carried out a more sophisticated version of the Monte Carlo analysis from our first method. In this case we relaxed the constraint requiring that the ratio u/q is fixed. This assumption is particularly poor when the u and q

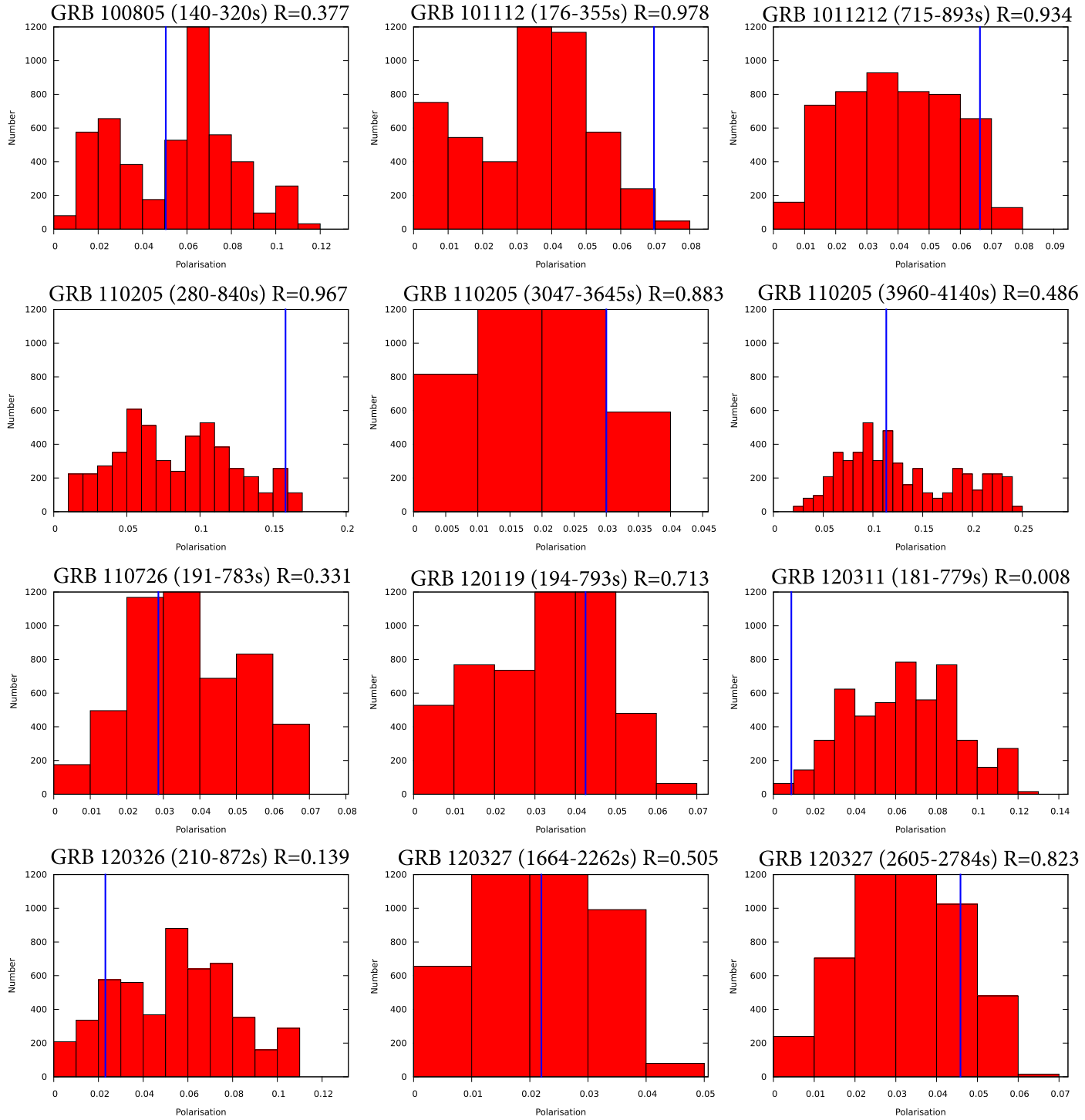

Figure 8. Distribution of possible polarization values for each GRB. The histograms are constructed using all possible permutations of the eight flux values measured for that GRB and have equal bin size $P = 1\%$. The data are corrected for both instrumental polarization and depolarization. The vertical (blue) line indicates the measured value for the GRB. The normalized rank (R) of the GRB within the distribution is indicated. For sources with $R < 0.9$ we conclude that the measured flux values are consistent with zero polarization and use the maximum permutated value to derive an upper limit.

error bars approach the origin and was imposed in the "all objects in all frames" analysis of Section 5.1 because of computational constraints. In this final analysis we therefore explored simulated ranges of polarization from 0.01% to 70.00% and EVPA from 0°.0 to 179°.9. The mean of the distribution of "valid" polarization and EVPA values were then taken as the final measured value (as opposed to simply applying Equations (3) and (4)). This procedure corrects for polarization bias (Simmons & Stewart 1985; Jermak et al. 2016), although the corrections are in any case small (<1%) compared to the measured values and their associated errors. The 10% and 90% limits of the distribution were used to define the error bars. For any particular burst, if the lower error bar reached zero, the upper error bar was interpreted as an upper limit. The results of this procedure are presented in Table 3.

Table 3
Polarization Results

GRB	$t - t_0$ (s)	P (%)	EVPA (deg)	Rank	Afterglow onset t_{peak} (s)	T90	$A_V^{Gal.}$	z
100805A	140–320	<14	⋯	0.377	<140.4	16.7	0.5	≈ 1.3
101112A	176–355	6^{+3}_{-2}	71 ± 10	0.978	299.0 ± 6.0	9.2	0.4	$\lesssim 3.5$
”	715–893	6^{+4}_{-3}	76 ± 15	0.934		”	”	”
110205A	240–840	13^{+13}_{-9}	126 ± 26	0.967	1027.0 ± 8.0	249	0.04	2.22
”	3047–3645	<5	⋯	0.883	”	”	”	”
”	3960–4140	<23	⋯	0.486	”	”	”	”
110726A	191–783	<14	⋯	0.331	<191.2	5.2	0.21	$1.04 < z < 2.7$
120119A	194–793	<8	⋯	0.713	<194.4	68.0	0.3	1.728
120308A	240–323	28 ± 4	34 ± 4	>0.99	298.0 ± 16.0	61.3	0.11	$2.22^{+0.25}_{-0.27}$
”	323–407	23 ± 4	44 ± 6	>0.99	”	”	”	”
”	407–491	17^{+4}_{-5}	51 ± 9	>0.99	”	”	”	”
”	491–575	16^{+4}_{-7}	40 ± 10	>0.99	”	”	”	”
”	575–827	16^{+4}_{-5}	55 ± 9	>0.99	”	”	”	”
120311A	181–779	<13	⋯	0.008	<180.6	3.5	0.37	$\lesssim 3$
120326A	210–872	<14	⋯	0.139	<216.0	69.5	0.14	1.798
120327A	1664–2263	<4	⋯	0.505	<1663.8	63.5	0.92	2.81
”	2605–2784	<7	⋯	0.823	”	”	”	”

Note. Columns are the GRB identifier, interval of RINGO2 observations, degree of polarization, measured polarization sky angle (east of north), rank of the polarization measurement in permutation analysis, optical afterglow peak time, gamma-ray emission duration, Galactic extinction in V band, and redshift.

6. Discussion

We fit the optical light curves of our nine afterglows with a simple power-law (PL) or/and a smoothly jointed broken PL function (B) (Beuermann et al. 1999). We followed the fitting procedure outlined in Kopač et al. (2013) ,where for each GRB we start by fitting a simple PL, and if the fit is not satisfactory, we add additional components: first a broken PL (B), then B plus single PL, and then finally two Beuermann functions. We always fit the complete optical data set simultaneously (i.e., all the filters at the same time, but assuming no color evolution, i.e., only a normalization change for each filter). In the case of the combined functions, a simple linear addition of the two components is made, with their relative contributions normalized via the PL fit parameters.

The fitting results (e.g., decay and rising indexes and peak times) are summarized in Table 4. The light curves of the four events GRB 100805A, GRB 120311A, GRB 120326A, and GRB 120327A are well modeled by a simple PL function, as shown in Figure 9. Although GRB 120326A indicates a very shallow decay with $\alpha_{decay} \sim 0.42$ (possibly due to refreshed shocks), the others are consistent with the standard forward-shock emission $\alpha_{decay} \sim 1$ (Sari et al. 1998). For these events, the duration T_{90} of the prompt gamma-rays are 3.5–70 s, and the optical observations started well after the end of the prompt gamma-ray emission phases. The observations were not prompt enough to detect the onset of afterglow, and the optical emission is dominated by the forward-shock emission in these observations. Since the forward-shock region is expected to contain only highly tangled magnetic fields generated around the shock (Medvedev & Loeb 1999; however, see also Uehara et al. 2012), the non-detection of polarization is consistent with the forward-shock model. We also plot in Figure 9 the X-ray light curves (black crosses). They indicate significant multiple flares in the early phase. These X-ray flares have been reported in many events, and the rapid variability $\Delta t/t$ indicates that these originate from internal dissipation processes, rather than forward shock, e.g., Nousek et al. (2006) and Zhang et al. (2006).

The other five events show a more complex behavior in the early optical afterglow, as shown in Figures 10 and 11. These light curves indicate a peak or/and rebrightening at later times. The three events for which we have detected polarization signals are all in this group:

1. GRB 101112A: we detected ∼6% polarization degree around the peak and in the decay phase $\alpha_{decay} \sim 1.1$. If the peak at $t_{peak} \sim 299$ s is the onset of the afterglow, considering $t_{peak} \gg T_{90} \sim 9.2$ s, this is a thin-shell case (Sari & Piran 1995; Kobayashi et al. 1999). The expected rising t^3 of the (slow-cooling) forward-shock emission is slower than the observed rising $\sim t^{4.2}$, and it implies that the reverse-shock emission contributed around the peak (Kobayashi 2000). Although the fast-cooling forward-shock emission can rise as rapidly as $\sim t^{3.7}$, the expected decay $t^{-1/4}$ after the peak that is due to the passage of the cooling frequency is very shallow, and it is not consistent with our observations.
2. GRB 110205A: the peak at $t_{peak} \sim 1027$ s ($\gg T_{90} = 249$ s) is considered to be the onset of the afterglow. The rapid rise $t^{4.6}$ and decay $t^{-1.5}$ implies the contribution to the peak from a reverse shock in the thin-shell regime. A polarization degree of 13% was detected in the rising phase.
3. GRB 120308A: we detected polarization degrees as high as 28% for this event. The high polarization was detected around the peak at $t_{peak} = 298$ s ($\gg T_{90} = 61.3$ s), and the very rapid rise t^5 and decay $t^{-2.4}$ are a clear signature of the reverse shock. Mundell et al. (2013) demonstrated that this light curve is best described by the combination of the two components, one from a reverse and the other from a forward shock.

We also note that we detected polarization in multiple epochs for GRB 101112A and GRB120308A, with a constant EVPA within the error limits in both cases.

Polarization signals were not detected from the remaining two events, which show peak or/and rebrightening in their afterglow light curves:

Table 4
Light Curve Fitting Results

GRB	Model[a]	Fit parameters	χ^2 (d.o.f.)
100805A	PL	$\alpha^{\rm PL}_{\rm decay} = 0.86 \pm 0.04$	30.8 (24)
101112A	B	$\alpha_{\rm rise} = -4.24 \pm 2.95$	19.4 (28)
		$\alpha_{\rm decay} = 1.10 \pm 0.05$	
		$t_{\rm peak} = 299 \pm 6$ s	
		$n = 0.86 \pm 0.72$	
110205A	B	$\alpha_{\rm rise} = -4.63 \pm 0.29$	220.5 (84)
		$\alpha_{\rm decay} = 1.52 \pm 0.02$	
		$t_{\rm peak} = 1027 \pm 8$ s	
		$n = 2.18 \pm 0.45$	
110726A	PL + B	$\alpha^{\rm PL}_{\rm decay} = 1.03 \pm 0.05$	32.1 (30)
		$\alpha_{\rm rise} = -7.87 \pm 21.21$	
		$\alpha_{\rm decay} = 1.13 \pm 0.33$	
		$t_{\rm peak} = 3256 \pm 185$ s	
		$n = 0.40 \pm 1.23$	
120119A	PL + B	$\alpha^{\rm PL}_{\rm decay} = 0.65 \pm 0.06$	105.8 (74)
		$\alpha_{\rm rise} = -1.06 \pm 0.41$	
		$\alpha_{\rm decay} = 1.68 \pm 0.19$	
		$t_{\rm peak} = 822 \pm 22$ s	
		$n = 1.05 \pm 0.48$	
120308A	B + B[b]	$\alpha^{1}_{\rm rise} = -5$	10.7 (17)
		$\alpha^{1}_{\rm decay} = 2.4 \pm 0.6$	
		$t^{1}_{\rm peak} = 298 \pm 16$ s	
		$n^{1} = 1$	
		$\alpha^{2}_{\rm rise} = -0.5$	
		$\alpha^{2}_{\rm decay} = 1.4 \pm 0.1$	
		$t^{2}_{\rm peak} = 730^{+190}_{-150}$ s	
		$n^{2} = 1$	
120311A	PL	$\alpha^{\rm PL}_{\rm decay} = 1.03 \pm 0.06$	12.7 (13)
120326A	PL	$\alpha^{\rm PL}_{\rm decay} = 0.42 \pm 0.04$	12.9 (12)
120327A	PL	$\alpha^{\rm PL}_{\rm decay} = 1.22 \pm 0.02$	25.2 (50)

Notes.
[a] PL is a simple power-law model ($F \propto t^{-\alpha}$, while B is a Beuermann model (smoothly joint broken power-law model, see Beuermann et al. 1999).
[b] Results from Mundell et al. (2013).

1. GRB 110726A: the light curve initially decays with $\alpha_{\rm decay} = 1.03$, and it shows a rebrightening around $t = 3200$ s. The polarization limits were obtained during the initial PL decay phase. The decay index is consistent with the forward-shock emission. Except for the rebrightening, which is possibly due to energy injection (Nousek et al. 2006; Zhang et al. 2006), this event looks similar to the PL events shown in Figure 9.
2. GRB 120119A: a broad peak is noticeable in the light curve. The rise is very slow, the I-band light curve is almost flat at the beginning. The polarization limit was obtained during the slow rising phase. This broad peak can be reasonably explained by forward-shock models with energy injection or density enhancement in the ambient medium (Nousek et al. 2006; Zhang et al. 2006).

Figure 12 shows the polarization measurements (detection or upper limit) of all nine events as a function of the observing time since the GRB trigger. We note that all polarization detection cases (GRB101112A, GRB110205A, and GRB120308A) were achieved at relatively early times $t < 10^3$ s. This reinforces the point that prompt measurements are essential to characterize the

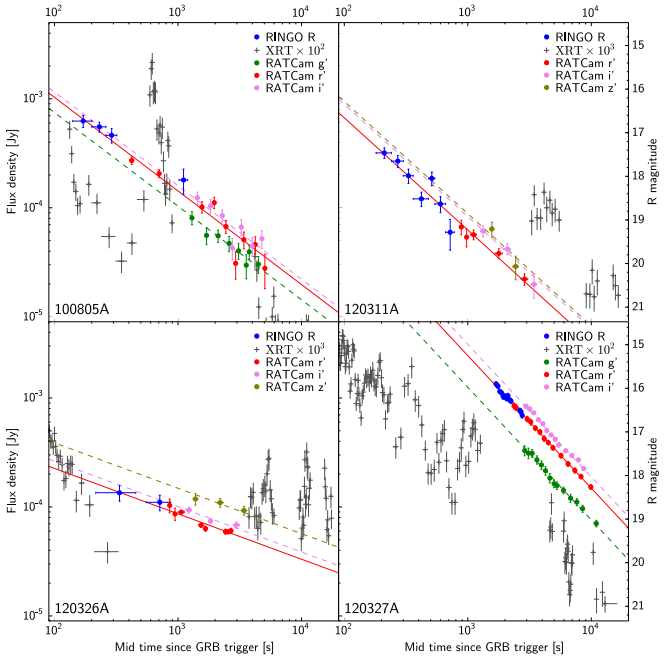

Figure 9. Light curves for GRB 100805A, GRB 120311A, GRB 120326A, and GRB 120327A, which show a single power-law decay morphology.

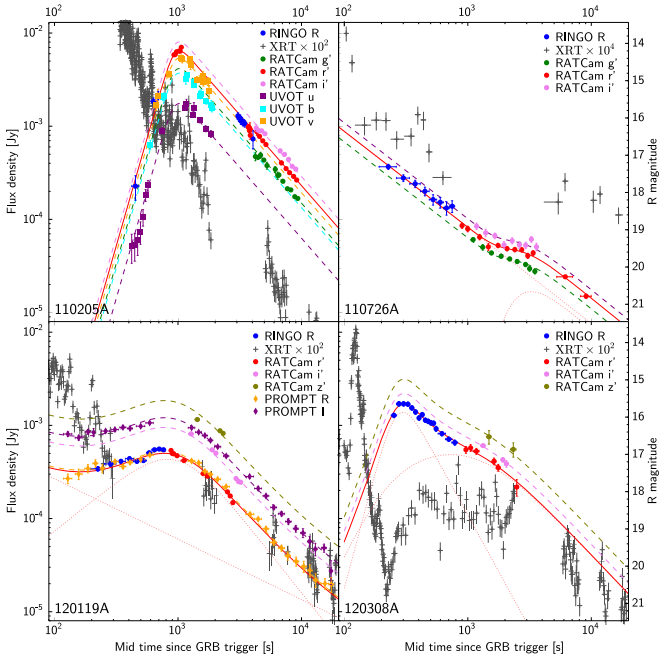

Figure 10. GRB 110205A, GRB 110726A, GRB 120119A, and GRB 120308A for which the light curves show definite structure. The Beuermann and PL components defined in Table 4 are plotted individually as dotted lines, and the final r-band model fit (the summation of the multiple components) is plotted as a solid line. To more easily compare the light-curve shape between filters by eye, the model is plotted multiple times offset to align with the non-r' band filters and plotted as a dashed line. The steep rise for GRB 110205A and GRB 120308A indicates the presence of the reverse-shock component in the afterglow.

polarimetric properties of GRB afterglow; the polarization degree decays very rapidly as the tight upper limits at late times show.

All polarized cases suggest the reverse-shock emission at early times. Since no new electrons are shocked after the reverse shock has crossed GRB ejecta, the reverse-shock emission is short lived, and it decays faster than the emission

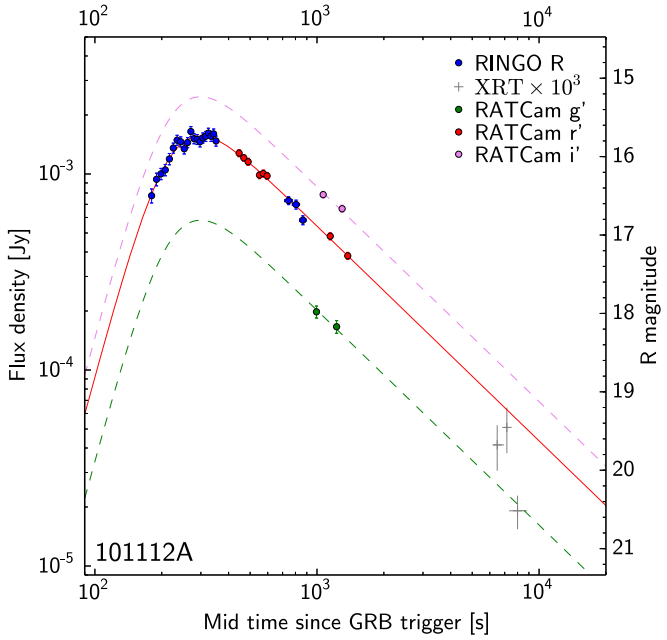

Figure 11. GRB 101112A light curve. The steep rise indicates the presence of the reverse-shock component, while the shallow decay indicates that reverse-shock and forward-shock components peak at similar times.

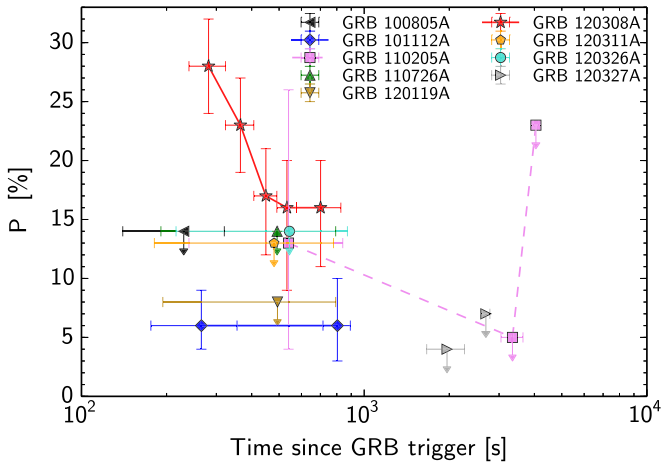

Figure 12. Polarization degree as a function of time after the burst for all nine GRBs from the RINGO2 sample. The temporal error bars show the duration of the exposure.

from the forward shock, which continuously shocks electrons in ambient medium. Therefore, a rapid decay, typically t^{-2}, is also a signature of the reverse-shock emission (Sari & Piran 1999; Kobayashi 2000; Zhang et al. 2003; Japelj et al. 2014). We therefore tested the correlation between the observed decay index and polarization degree. Figure 13 shows that the polarized cases (the green crosses) do indeed have larger decay indexes. The light curve of GRB120308A shows a double-peak structure with reverse- and forward-shock peaks at different times. The polarization degree is much higher during the clearly separated reverse-shock peak. However, for GRB 110205A, the polarization $P = 13\%$ is detected only in the rising phase, and we have tight upper limits of $P < 5\%$ in the decay phase ($\alpha_{\rm decay} = 1.52$).

Zheng et al. (2012) showed that the full optical and x-ray afterglow of GRB 110205A could be interpreted within the

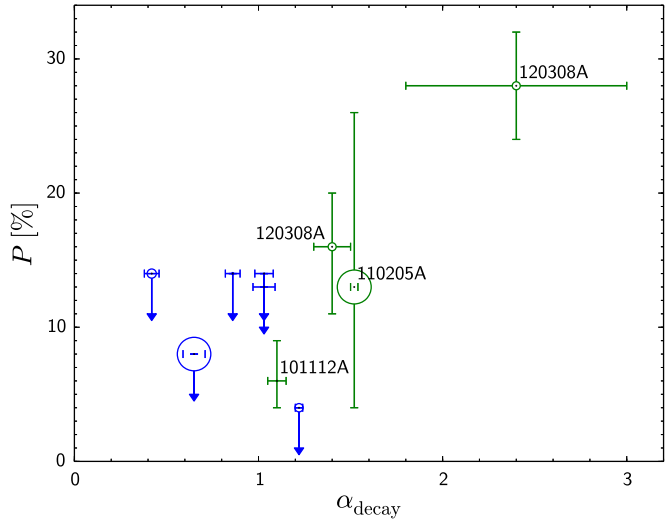

Figure 13. . PL decay index (α) vs. degree of polarization. The green points in the plot are measurements, while blue points are upper limits. The relative size of the point is the T90 value (which shows no correlation with α or and P). For GRB120308A we plot two epochs: (240–323 s, $P = 28\%$) and (575–827 s, $P = 16\%$).

standard reverse-shock plus forward-shock model, and they proposed two scenarios. Scenario I invokes both the forward shock and reverse shock to peak at $\sim 10^3$ s, while scenario II invokes the reverse shock only for the peak at $\sim 10^3$ s, with the forward-shock peak later when the typical frequency crosses the optical band. According to their modeling (see Figure 5 in their paper), the reverse-shock contribution becomes negligible by our polarization observations around 3000–3600 s. Our limit $P < 5\%$ is consistent with the dominance of the forward-shock emission in the optical band. In scenario II, the optical band is still dominated by the reverse-shock emission in the observation period. Because of the relativistic beaming effect, we can see only a small portion of the GRB ejecta just around the line of sight with an angular scale of $1/\Gamma_0 \sim 4 \times 10^{-3}$, where $\Gamma_0 \sim 250$ is the initial Lorentz factor of the ejecta (Zheng et al. 2012). After the reverse-shock crossing, the ejecta rapidly decelerates as $\Gamma \propto R^{-g} \sim R^{-2}$ in terms of the ejecta radius (Kobayashi & Sari 2000). However, it is not so rapid in terms of the time $\Gamma \propto t^{-g/(1+2g)} \propto t^{-0.4}$. By $t \sim 3000$ s, the angular size of the visible region grows only by a factor of $\sim 3^{0.4} \sim 1.6$, compared to the size at the peak time $t \sim 10^3$ s. Although a larger visible region at a later time potentially reduces the polarization degree if the magnetic fields have an irregularity in the angular scale of $1/\Gamma_0$ or a slightly larger scale, this small change in the size does not explain the drastic change from $P = 13\%$ to $P < 5\%$. Our polarization measurements therefore disfavor scenario II.

7. Conclusion

We have presented the complete RINGO2 catalog of GRB afterglow observations. We carried out 19 prompt RINGO2 observations between 2010 and 2012. Nine out of the 19 events were bright enough to perform polarimetric analysis, the polarization degrees (or limits) and EVPA were measured. We detected polarization signals in their early optical afterglow for three events: GRB 101112A, GRB110205A, and GRB120308A. Using RINGO2 and RATCam data, we constructed the light curves of the bright events to evaluate the decay indexes of the afterglow. The combination of our photometric and polarimetric

Table 5
RINGO2 Sample Complete Photometry

GRB	t_{start} (minutes)	Exp (s)	Filter	Magnitude	F_{ν}^{OPT} (mJy)
100805A	2.34	60.6	RINGO r'	17.29 ± 0.13	0.653 ± 0.078
	3.35	59.9	RINGO r'	17.42 ± 0.11	0.579 ± 0.061
	4.35	58.7	RINGO r'	17.62 ± 0.16	0.484 ± 0.069
	16.99	178.9	RINGO r'	18.66 ± 0.28	0.190 ± 0.048
	6.78	30.0	RATCam r'	18.24 ± 0.09	0.271 ± 0.021
	11.49	30.0	RATCam r'	18.54 ± 0.09	0.206 ± 0.017
	25.82	30.0	RATCam r'	19.31 ± 0.13	0.102 ± 0.012
	32.53	30.0	RATCam r'	19.21 ± 0.13	0.111 ± 0.013
	40.18	60.0	RATCam r'	19.76 ± 0.15	0.067 ± 0.009
	48.33	60.0	RATCam r'	20.64 ± 0.32	0.031 ± 0.009
	56.43	60.0	RATCam r'	20.07 ± 0.19	0.051 ± 0.009
	69.38	120.0	RATCam r'	20.18 ± 0.19	0.046 ± 0.008
	82.70	180.0	RATCam r'	20.78 ± 0.40	0.028 ± 0.010
	21.38	30.0	RATCam g'	19.75 ± 0.15	0.081 ± 0.011
	28.12	30.0	RATCam g'	20.16 ± 0.19	0.056 ± 0.010
	34.73	60.0	RATCam g'	20.16 ± 0.14	0.055 ± 0.007
	42.76	60.0	RATCam g'	20.34 ± 0.17	0.047 ± 0.008
	51.05	60.0	RATCam g'	20.51 ± 0.18	0.040 ± 0.007
	59.00	60.0	RATCam g'	20.86 ± 0.28	0.030 ± 0.007
	61.92	120.0	RATCam g'	20.53 ± 0.16	0.039 ± 0.006
	73.11	180.0	RATCam g'	20.82 ± 0.19	0.030 ± 0.005
	23.68	30.0	RATCam i'	18.99 ± 0.14	0.124 ± 0.016
	30.33	30.0	RATCam i'	19.18 ± 0.16	0.104 ± 0.015
	37.53	60.0	RATCam i'	19.40 ± 0.14	0.085 ± 0.011
	45.40	60.0	RATCam i'	20.16 ± 0.25	0.043 ± 0.010
	53.78	60.0	RATCam i'	19.67 ± 0.18	0.067 ± 0.011
	65.57	120.0	RATCam i'	20.11 ± 0.21	0.045 ± 0.009
	78.10	180.0	RATCam i'	19.94 ± 0.20	0.052 ± 0.010

Note. Magnitudes are corrected for Galactic extinction.

(This table is available in its entirety in machine-readable form.)

data have shown that there is a correlation between decay index and polarization degree, i.e., polarized events decay faster. This clearly indicates that the events for which polarization were detected have a reverse-shock emission component in the early afterglow.

The internal energy produced by shocks is believed to be radiated via synchrotron emission. The presence of strong magnetic fields is crucial in the standard synchrotron shock model. Although magnetic fields are usually assumed to be generated locally by instabilities in shocks, with the resulting tangled fields, the polarization signals are canceled out. The polarized reverse-shock emission indicates that there are large-scale magnetic fields in the original GRB ejecta that are likely to be generated at the GRB central engine. We have detected polarization signals in multiple epochs for two events: GRB 101112A and GRB120308A. In the former case, the polarization degree is constant around the onset of afterglow and in the decay phase. The latter shows the gradual decay of the polarization signals. EVPA remains constant within the error limits in both cases. In magnetic GRB jet models that assume the amplification of magnetic fields by the rotation of the central black hole and the accretion disk, the outflow is expected to be threaded with globally ordered magnetic fields that are likely to be dominated by a toroidal component, because the radial field decays faster than the tangential field. Although the toroidal fields can be distorted by internal dissipation processes preceding the onset of afterglow, e.g., Zhang & Yan (2011), the visible region with angular scale $\sim 1/\Gamma$ might have a rather uniform magnetic field, and the polarization (electric) vector is expected to point toward the jet axis. The constant EVPA results are consistent with this model.

As illustrated especially in the cases of GRB 110205A and GRB 120308A, polarimetry allowed us to carry out the detailed modeling of early afterglow. Polarization measurements can distinguish the forward-shock and reverse-shock emission components. Since the reverse-shock emission is short lived, prompt polarization measurements at less than $t \sim 10^3$ s are essential to fully characterize the early afterglow and constrain the GRB central engine (Kopač et al. 2015).

The Liverpool Telescope is operated on the island of La Palma by Liverpool John Moores University in the Spanish Observatorio del Roque de los Muchachos of the Instituto de Astrofisica de Canarias with financial support from the UK Science and Technology Facilities Council (STFC). C.G.M. acknowledges support from the Royal Society, the Wolfson Foundation, and STFC. D.K. acknowledges the financial support from the Slovenian Research Agency (research core funding No. P1-0188).

References

Arnold, D. M. 2017, PhD thesis, Liverpool JMU
Bersier, D. 2012, GCN, 13320
Bertin, E., & Arnouts, S. 1996, A&A, 117, 393
Beuermann, K., Hessman, F. V., Reinsch, K., et al. 1999, A&A, 352, L26

Breeveld, A. A., Landsman, W., Holland, S. T., et al. 2011, in AIP Conf. Ser 1358, ed. J. E. McEnery, J. L. Racusin, & N. Gehrels (Melville, NY: AIP), 373
Cenko, S. B., Hora, J. L., & Bloom, J. S. 2011, GCN, 11638
Clarke, D., & Neumayer, D. 2002, A&A, 383, 360
Covino, S., Lazzati, D., Ghisellini, G., et al. 1999, A&A, 348, L1
Cox, L. J. 1976, MNRAS, 176, 525
Cucchiara, A., Bloom, J. S., & Cenko, S. B. 2011a, GCN, 12202
Cucchiara, A., Cenko, S. B., Bloom, J. S., et al. 2011b, ApJ, 743, 154
Cucchiara, A., & Prochaska, J. X. 2012, GCN, 12865
D'Avanzo, P., Milvang-Jensen, B., Vreeswijk, P., et al. 2012, GCN, 13051
Fukugita, M., Shimasaku, K., & Ichikawa, T. 1995, PASP, 107, 945
Ghisellini, G., & Lazzati, D. 1999, MNRAS, 309, L7
Goldstein, A. 2010, GCN, 11403
Granot, J., Piran, T., Bromberg, O., Racusin, J. L., & Daigne, F. 2015, SSRv, 191, 471
Guidorzi, C., & Melandri, A. 2012, GCN, 13092
Guidorzi, C., Melandri, A., Steele, I. A., et al. 2011, GCN, 11537
Guidorzi, C., Monfardini, A., Gomboc, A., et al. 2006, PASP, 118, 288
Guidorzi, C., & Mundell, C. G. 2012, GCN, 13651
Guidorzi, C., Smith, R. J., Mundell, C. G., et al. 2010, GCN, 11397
Holland, S. T., & Hoversten, E. A. 2010, GCN, 11062
Japelj, J., Kopač, D., Kobayashi, S., et al. 2014, ApJ, 785, 84
Jermak, H., Steele, I. A., Lindfors, E., et al. 2016, MNRAS, 462, 4267
Jermak, H. E. 2016, PhD thesis, Liverpool JMU
Jordi, K., Grebel, E. K., & Ammon, K. 2006, A&A, 460, 339
Klotz, A., Gendre, B., Boer, M., & Atteia, J. L. 2011, GCN, 12022
Klotz, A., Gendre, B., Boer, M., & Atteia, J. L. 2012, GCN, 13290
Kobayashi, S. 2000, ApJ, 545, 807
Kobayashi, S., Piran, T., & Sari, R. 1999, ApJ, 513, 669
Kobayashi, S., & Sari, R. 2000, ApJ, 542, 819
Komissarov, S. S., Vlahakis, N., Königl, A., & Barkov, M. V. 2009, MNRAS, 394, 1182
Kopač, D., Kobayashi, S., Gomboc, A., et al. 2013, ApJ, 772, 73
Kopač, D., Mundell, C. G., Japelj, J., et al. 2015, ApJ, 813, 1
Kuroda, D., Hanayama, H., Miyaji, T., et al. 2012, GCN, 13465
Lacluyze, A., Maturi, M., Ivarsen, K., et al. 2011, GCN, 12024
Lazzati, D., Rossi, E., Ghisellini, G., & Rees, M. J. 2004, MNRAS, 347, L1
Lien, A., Sakamoto, T., Barthelmy, S. D., et al. 2016, ApJ, 829, 7
Lin, H.-N., Li, X., & Chang, Z. 2017, ChPhC, 41, 045101
Medvedev, M. V., & Loeb, A. 1999, ApJ, 526, 697
Melandri, A., Virgili, F. J., Guidorzi, C., et al. 2014, A&A, 572, A55
Morgan, A. N., Perley, D. A., Cenko, S. B., et al. 2014, MNRAS, 440, 1810
Mundell, C. G., Kopač, D., Arnold, D. M., et al. 2013, Natur, 504, 119
Mundell, C. G., Melandri, A., & Tanvir, N. 2011, GCN, 11858
Naghizadeh-Khouei, J., & Clarke, D. 1993, A&A, 274, 968
Nava, L., Nakar, E., & Piran, T. 2016, MNRAS, 455, 1594
Nousek, J. A., Kouveliotou, C., Grupe, D., et al. 2006, ApJ, 642, 389
Papoulis, A. 1984, Probability, Random Variables and Stochastic Processes (2nd ed.; New York: McGraw-Hill)
Perley, D. A., & Tanvir, N. R. 2012, GCN, 13133
Piran, T. 1999, PhR, 314, 575
Rossi, E. M., Lazzati, D., Salmonson, J. D., & Ghisellini, G. 2004, MNRAS, 354, 86
Sari, R. 1999, ApJL, 524, L43
Sari, R., & Piran, T. 1995, ApJL, 455, L143
Sari, R., & Piran, T. 1999, ApJL, 517, L109
Sari, R., Piran, T., & Narayan, R. 1998, ApJL, 497, L17
Schlafly, E. F., & Finkbeiner, D. P. 2011, ApJ, 737, 103
Schmidt, G. D., Elston, R., & Lupie, O. L. 1992, AJ, 104, 1563
Simmons, J. F. L., & Stewart, B. G. 1985, A&A, 142, 100
Smith, J. A., Tucker, D. L., Kent, S., et al. 2002, AJ, 123, 2121
Steele, I. A. 2001, AN, 322, 307
Steele, I. A., Bates, S. D., Carter, D., et al. 2006, Proc. SPIE, 6269, 62695M
Steele, I. A., Bates, S. D., Guidorzi, C., et al. 2010, Proc. SPIE, 7735, 773549
Steele, I. A., Mottram, C. J., Smith, R. J., & Barnsley, R. M. 2014, Proc. SPIE, 9154, 915428
Steele, I. A., Mundell, C. G., Smith, R. J., Kobayashi, S., & Guidorzi, C. 2009, Natur, 462, 767
Steele, I. A., Smith, R. J., Rees, P. C., et al. 2004, Proc. SPIE, 5489, 679
Tello, J. C., Sanchez-Ramirez, R., Gorosabel, J., et al. 2012, GCN, 13118
Turnshek, D. A., Bohlin, R. C., Williamson, R. L., II, et al. 1990, AJ, 99, 1243
Uehara, T., Toma, K., Kawabata, K. S., et al. 2012, ApJL, 752, L6
Virgili, F. J., Guidorzi, C., Melandri, A., & Mundell, C. G. 2012, GCN, 13006
Wiersema, K., Covino, S., Toma, K., et al. 2014, Natur, 509, 201
Wijers, R. A. M. J., Vreeswijk, P. M., Galama, T. J., et al. 1999, ApJL, 523, L33
Yonetoku, D., Murakami, T., Gunji, S., et al. 2011, ApJL, 743, L30
Zhang, B., Fan, Y. Z., Dyks, J., et al. 2006, ApJ, 642, 354
Zhang, B., Kobayashi, S., & Mészáros, P. 2003, ApJ, 595, 950
Zhang, B., & Mészáros, P. 2004, IJMPA, 19, 2385
Zhang, B., & Yan, H. 2011, ApJ, 726, 90
Zheng, W., Shen, R. F., Sakamoto, T., et al. 2012, ApJ, 751, 90